BioNanoScience (2023) 13:958–972
https://doi.org/10.1007/s12668-023-01130-0

Copper Ferrite Nanoparticles: Structural, Magnetic, Optical, Photocatalytic Activity and Blood Compatibility Properties

Sezen Özçelik[1]

Accepted: 11 May 2023 / Published online: 19 May 2023
© The Author(s), under exclusive licence to Springer Science+Business Media, LLC, part of Springer Nature 2023

Abstract

In this study, $CuFe_2O_4$ nanoparticles (NPs) have been successfully synthesized via the co-precipitation method. Based on chemical composition and considering biological properties of $CuFe_2O_4$ ferrites nanoparticles, the structural, magnetic, photocatalytic and biocompatibility properties were investigated. X-ray diffraction analysis (XRD), scanning electron microscope (SEM), and UV–vis diffuse reflectance (DRS) spectrum techniques have been employed to analyze the structural and morphological properties of nanoparticles. By using the XRD results, it was found that the NPs have a cubic structure with a space group *Fd3m*. From UV–visible measurement, the direct and indirect gap energies of the Cu-ferrite NPs samples were obtained as 3.24 and 2.6 eV, respectively. Photocatalytic activity tests have showed that $CuFe_2O_4$ nanoparticles could degrade 55.4% of total organic dye after 1440 min of the model dye. Characteristics of the absorbance spectra obtained from hemolysis tests also revealed the possible interactions of copper and thiol (–SH) groups. Moreover, the observation of the formation of a characteristic black precipitate in hemolytic activity tests was interpreted as clear evidence for the formation of heme–iron complexes. The M-H loop shows a *S*-shaped pointing to the soft ferromagnetic behavior with the coercivity field (H_c) value of 1412 Oe, saturation magnetization (*Ms)* value of 14.06 emu/gr.

Keywords Spinel Ferrite · Nano particles · Microstructure · Photocatalysis · Blood compatibility

1 Introduction

The synthesis and the investigations of magnetic nano particles have been playing an important role in several application areas, such as catalyst, semiconductors, sensors, nanodevices, microwave devices, MR imaging, high-density magnetic storage, and controlled drug delivery, biomedical, and pigment applications [1–14]. Among the magnetic nano-sized materials, in addition to iron oxide, other iron-containing materials also possess the magnetic properties required for biomedical applications. Ferrites are materials that are extremely valuable and suitable for other application areas such as MRI and magnetic hyperthermia thanks to the control of their physicochemical properties using an external magnetic field [15, 16].

The nanoparticles (NPs) planned to be used for such applications are desired to exhibit low toxicity, have high structural stability, and have pronounced super-paramagnetic properties at room temperature (RT). For example, it has been emphasized in some studies that NPs displaying super-paramagnetic properties are biocompatible against erythrocytes [2, 3], and various cells with cancer (for example breast and lungs) [5] even without using immune-specific coatings.

Among the magnetic nanoparticles, the spinel ferrites (SFs) are shown by the chemical formula of MFe_2O_4 where M refers to a divalent cation such as Co, Cu, Fe, Mn, or Ni. Among SFs, especially cobalt ferrite ($CoFe_2O_4$) and copper ferrite ($CuFe_2O_4$) is the focus of attention in physical, chemical, and medical aspects due to their high coercivity, significant mechanical and chemical stability, and high magneto-crystalline anisotropy [17–19]. According to the preparation technique and sintering temperature, $CuFe_2O_4$ is constituted in two crystal structures namely cubic spinel and tetragonal form. General producing techniques of nanoparticles are known as hydrothermal [20], sonochemical [21], citrate–nitrate [22, 23], sol–gel [24], co-precipitation [25, 26], and solid-state [27] ones. Recently, $CuFe_2O_4$ structural materials having different morphologies have been studied

---

✉ Sezen Özçelik
sezenozcelik86@gmail.com

[1] Faculty of Engineering, Department of Food Engineering, Hakkari University, 30000 Hakkari, Turkey

and reported. These are nanoparticles [24], nanospheres [28], nanofibers [29], nanotubes [30], nanorings [30], nanorods [31], and honeycomb structures [32]. Up to now, $CuFe_2O_4$ spinel is widely used in different fields including heterogeneous catalysis [15, 16], photocatalysis [15], photocatalytic H_2 evolution activity [33], energy storage [20], anode material for batteries [24], high-density magnetic storage, for high-performance spintronic devices [34, 35]. Additionally, its usage is further extended to photocatalytic degradation of methylene blue [20], photocatalytic efficiency of in the decolorization of methylene blu [19], biomedicine and drug delivery [36], magnetic resonance imaging [37], magnetic separation of cancer cells, and antibacterial activities [38].

Although copper is an essential micronutrient also the co-factor of several enzymes involved in human metabolism, it shows toxic effects at elevated concentrations. This study also identifies the potential effectiveness of $CuFe_2O_4$ NPs in degradation reactions of organic molecules by photodegradation. For this purpose, photocatalytic activity of $CuFe_2O_4$ NPs towards crystal violet (CV) was studied. There are various studies which have been focused on catalytic properties of nano-structured metal oxide catalysts [11–14]. Nonetheless, the catalytic properties of pure $CuFe_2O_4$ NPs have not been investigated in previously reported studies.

Moreover, synthetic materials affect the morphology and physiology of blood cells and may change blood parameters. In medical research and diagnosis, as precursor symptoms, changes in blood parameters that indicate pathology are followed. Destruction of cell membrane and lysis of red blood cells which is defined as hemolysis is an undesirable result of nanoparticle-blood interactions. Reactive oxygen species (ROS) produced by the NPs can cause the immune system to be suppressed, causing various autoimmune disorders or infections. ROS are also recognized as responsible for the occurrence of various types of cancer. NPs may cause tissue inflammation and altered cellular functions through oxidation, leading to abnormal cell function or even cell necrosis. However, ferrites exhibit structural stability under physiological conditions and have adjustable superparamagnetic behavior [39] making these nano-sized particles a tough competitor over traditional iron oxide such as Fe_3O_4 and Fe_2O_3. The incompatibility of traditional iron oxides against erythrocytes due to the iron in their structure can be prevented by ferrites that provide better hemocompatibility.

In order to fabricate the spinel ferrites, several production techniques like sol–gel, ball milling, hydrothermal, thermal decomposition, solvothermal, and co-precipitation, [40–44] have been used. For nanoparticles synthesis, generally among these techniques, the co-precipitation one is preferred for its simplicity, being fast and economical. In addition, by altering the precursors and environmental conditions, the physical and chemical properties of precipitated nanoparticles can be managed. So, high purity nanoparticles suitable for magnetic characterization can be fabricated via controlling the preconditions. Spinel ferrites were considered as high-potential materials especially for bioimaging applications [18, 19]. Nevertheless, the mutual effect between nano particle ferrites and blood modules are still an unknown issue. Therefore, in this study, I have deeply focused to report the synthesis and material properties of $CuFe_2O_4$ nanoparticles and to investigate their photocatalytic and biocompatibility as well as having non-hemolytic nature which have not adequately been reported by using crystal violet (CV).

2 Experimental Procedures

2.1 Nanoparticle Synthesis

The co-precipitation method was used to prepare $CuFe_2O_4$ NPs. To fabricate nanocrystalline Cu-NPs, iron(III) nitrate nonahydrate ($FeN_3O_9.9H_2O$), and copper (II) nitrate hexahydrate ($Cu(NO_3)_2.6H_2O$) which are of analytical graded Alfa Aesar, were preferred. In the experimental procedure the weights of $FeN_3O_9.9H_2O$; $Cu(NO_3)_2.6H_2O$ chemicals were stated in accordance of the stoichiometry between ferrite and nitrates. First, the mixture of 0.2 molar $FeN_3O_9.9H_2O$ and 0.1 molar of $Cu(NO_3)_2.6H_2O$ was dissolved in deionizing water of 100 mL. Then, approximately 30 μL of oleic acid was dropped into the solution as an active agent (surfactant). For homogeneous and uniform temperature distribution, the solutions were mixed in an ultrasonic homogenizer (Bandaline Sonopuls model) at a fix temperature of 80 °C in the water for 2 h in a continuous mode. Then, in order to reach to 9 of pH value, the NaOH solution was added by slow degrees in 1-h time. Finally, the remaining precipitates were centrifuged in distilled water with the aid of the NUVE NF400 model five times at 5000 rpm for 10 min. Finally, in order to obtain nanoparticles of $CuFe_2O_4$, all precipitates were desiccated at 80 °C under vacuum for 8 h and calcinated at a temperature value of 500 °C under air condition for 2 h, respectively. The diagrammatic flow chart of synthesis process has presented in Fig. 1.

2.2 Structural, Optical, and Magnetic Analysis

XRD measurements using a PANalytical X'pert Powder3 model X-ray diffractometer device with CuKα ($\lambda = 1.5418$) radiation at RT in the scan range of $2\theta = 10°–70°$ with a scan speed of 3°/min and a step increment of 0.02° were carried out to characterize the structure of the $CuFe_2O_4$ ferrite NPs. A scanning electron microscope (SEM) of the Zeiss EVO MA model was used for analyzing the surface and morphological structure. To measure the optical properties of the

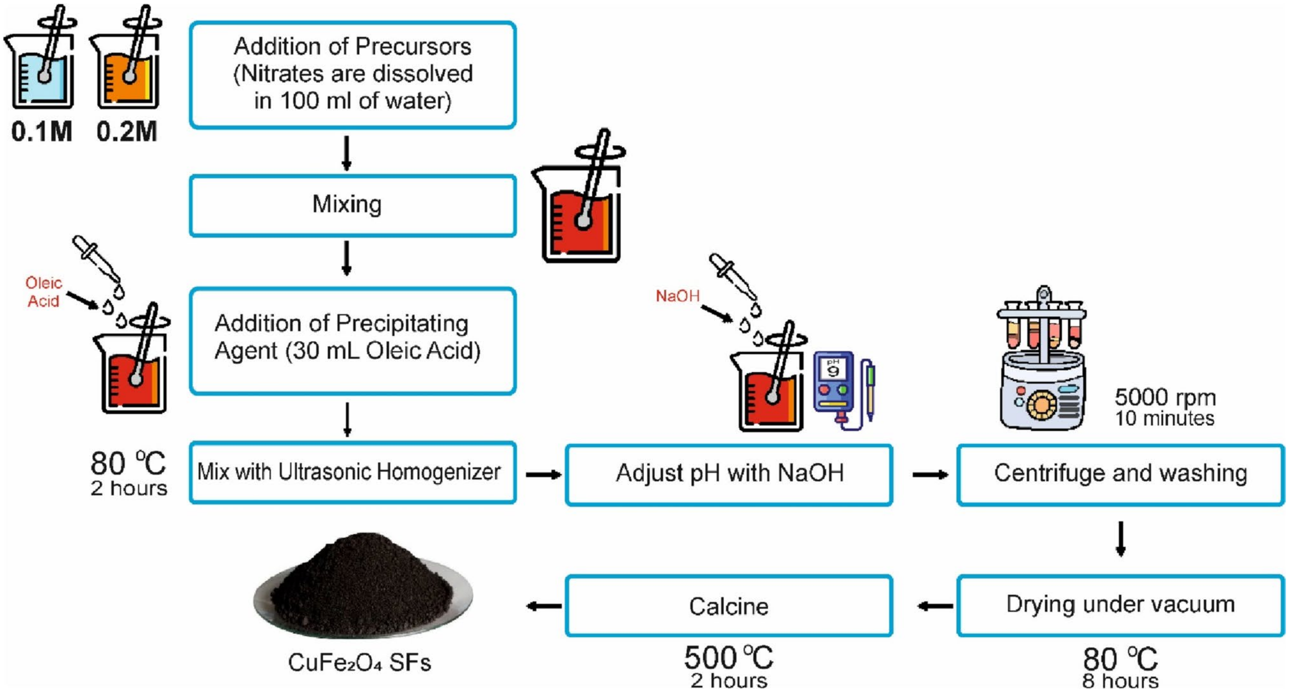

Fig. 1 The diagrammatic flow chart of synthesis process

$CuFe_2O_4$ NPs, a UV-Spectrometer (2600 Shimadzu mark) with an integrating sphere in 300-–1000-nm wavelength range was used. A Lake Shore model 7304 vibrating sample magnetometer operating within the 15–300 K temperature range was used to do magnetic hysteresis experiments.

2.3 Photocatalytic Activity Measurements

Photodegradation of crystal violet (CV) under 254-nm irradiation was carried out to evaluate the photocatalytic properties of Cu ferrite NPs. Nanoparticle dispersions and CV solution were prepared in distilled water at 1.0 mg/ml and 2.5×10^{-6} M respectively. The following procedure was applied to determine the photocatalytic performance of $CuFe_2O_4$ ferrites [45]. A homogeneous suspension was prepared by dispersing the appropriate number of NPs in the pre-prepared CV solution in the selected concentration. Before irradiation, magnetic stirring was applied to the nanoparticle-CV dispersions in the dark for 30 min to create the adsorption/desorption balance of the organic dye molecules on the surface of the NPs. Once adsorption equilibrium was established, I irradiated by continuously stirring aqueous dispersions of NPs under 254-nm irradiation. 1.5-ml aliquots were withdrawn at appropriate time intervals and centrifugation (4000 rpm for 3 min) was used to precipitate suspended NPs. A spectrophotometer with a 591-nm wavelength in connection with the absorption maxima of CV was selected to measure the absorption spectra of the supernatant. I used distilled water as a reference.

2.4 Blood Compatibility Tests

I collected venous blood samples from healthy volunteer to investigate $CuFe_2O_4$ ferrites for their hemolytic activity. I used an aqueous solution of 3.2% trisodium citrate as an anticoagulant to avoid the coagulation of entire blood examples. Whole blood samples anticoagulated with trisodium citrate (9:1) were diluted with calcium and magnesium-free phosphate buffer solution (PBS-pH7.35) and centrifuged at 4000 rpm for 5 min. Then, the supernatant was discharged, and I separated erythrocytes (red blood cells-RBCs) from plasma and diluted them up to 50 ml with PBS. Then, I added 0.8 ml of this RBC stock solution to 5.0 ml of $CuFe_2O_4$ nanoparticle suspensions with two different concentrations (1.0 mg/ml and 5.0 mg/ml). Distilled deionized water (DDW) and phosphate buffer solution were used to cause complete (100%) hemolysis (negative control) and 0% hemolysis (positive control), respectively.

I incubated nanoparticle-RBC dispersions at physiological temperature (37 °C) for 3 h under magnetic stirring. I tested replicates of the sample and then I centrifuged dispersions at 3000 rpm for 5 min. A UV–visible spectrophotometer to indicate hemoglobin release into the medium following erythrocytes lysis was used to record the absorbance of the supernatant from 200 to 800 nm. I calculated percent hemolysis values using the absorbance value (ABS) of the supernatant solution at 540 nm corresponding to the absorption maxima of oxyhemoglobin via the below equation [46];

$$\% \, Hemolysis = \frac{ABS_{test\ sample} - ABS_{negative\ control}}{ABS_{positive\ control} - ABS_{negative\ control}} \times 100 \tag{1}$$

3 Results and Discussions

3.1 XRD analysis

The X-ray diffraction (XRD) measurements were employed to obtain the crystallinity properties of $CuFe_2O_4$ ferrite NPs. In Fig. 2, All peaks illustrate almost the single phase of $CuFe_2O_4$ spinel corresponding to JCPDS Card No: 98–003-7429. The NPs have a cubic structure [10, 18] with a space group *Fd3m* and few secondary phases (CuO and Fe_2O_3) having very low intensities were observed. The unit cell parameter, a, was calculated via Eq. 2 [47], by using the diffraction patterns observed in XRD results.

$$a_{exp} = d_{hkl}\left(h^2 + k^2 + l^2\right)^{1/2} \tag{2}$$

By using the sharpest peak corresponding to (*311*) plane in the XRD patterns, the crystallite size of $CuFe_2O_4$ NPs was calculated from the well-known Debye–Scherrer equation given in Eq. 3 [47];

$$D = 0.9\lambda / \beta cos\theta_B \tag{3}$$

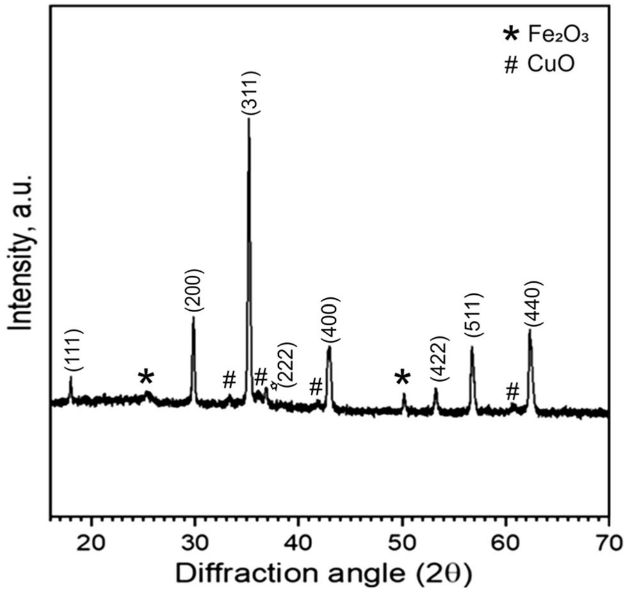

Fig. 2 XRD patterns of $CuFe_2O_4$ ferrite NPs

where λ is wavelength, β is the full width at half maximum intensity related to sharpest peak θ_B is the diffraction angle of the peak. The maximum crystallite thickness, D, and the unit cell parameter, a, values of $CuFe_2O_4$ NPs for (*311*) peaks are calculated as 38.04 nm and 8.45 Å, respectively. The obtained results are consistent with the literature [18, 24]

3.2 SEM Analysis

Scanning electron microscope was used to study the morphology of $CuFe_2O_4$ NPs as shown in Fig. 3. As can be seen from Fig. 3a–d, the $CuFe_2O_4$ NPs do not have a full shape due to the agglomeration. With decreasing resolution, the structure appears to be denser and more molten (Fig. 3c, d). Figure 4 illustrates the basic composition of $CuFe_2O_4$ NPs obtained by the EDS analysis. All peaks in EDS analysis indicate $CuFe_2O_4$ NPs and no extra different disagreeable elemental peak were observed.

3.3 Band Gap Calculation

I used UV–VIS diffuse reflectance measurements (DRS) to get the reflectance spectra of the $CuFe_2O_4$ NPs in the range of 0-–700-nm wavelength. An absorption edge in the vicinity of 370 nm appeared as illustrated in an inset in Fig. 5a. The reflection ratio F(R) was calculated using the Kubelka–Munk function [2]

$$F(R) = \frac{(1-R)^2}{2R} \tag{4}$$

I used the following equation to calculate the optical band gap E_g for the photon energy ($h\nu$) and the absorption coefficient (α):

$$\alpha h\upsilon = \mathrm{k}(\mathrm{h}\upsilon - E_g)^{1/n} \tag{5}$$

where k is an energy-independent constant. Since $F\left(R_\alpha\right)$ is proportional to $\boldsymbol{\alpha}$ and $\boldsymbol{n}$ is a constant that depends on the bandgap type *1/2* and *2* for direct and indirect bandgaps, respectively. Thus, Eq. (5) can be converted the following equations:

$$\begin{aligned} \left(F\left(R_\alpha\right)h\upsilon\right)^2 &= k\left(\mathrm{h}\upsilon - E_g\right) \text{ for direct transitions} \\ \left(F\left(R_\alpha\right)h\upsilon\right)^{1/2} &= k\left(\mathrm{h}\upsilon - E_g\right) \text{ for indirect transitions} \end{aligned} \tag{6}$$

Figure 5 shows the direct and indirect bandgap energy E_g which were calculated by the linear approximation of the slope of the graph of $(\mathrm{F(R_\alpha)\,h\upsilon})^2$ to the photon energy axis where $\mathrm{F(R_\alpha)} = 0$, namely, $E_g = h\upsilon$. The direct and indirect gap energies of the Cu-ferrite NPs samples were observed as 3.24 and 2.6 eV, respectively. The bandgap, E_g, values were influenced by few factors related to carrier concentrations,

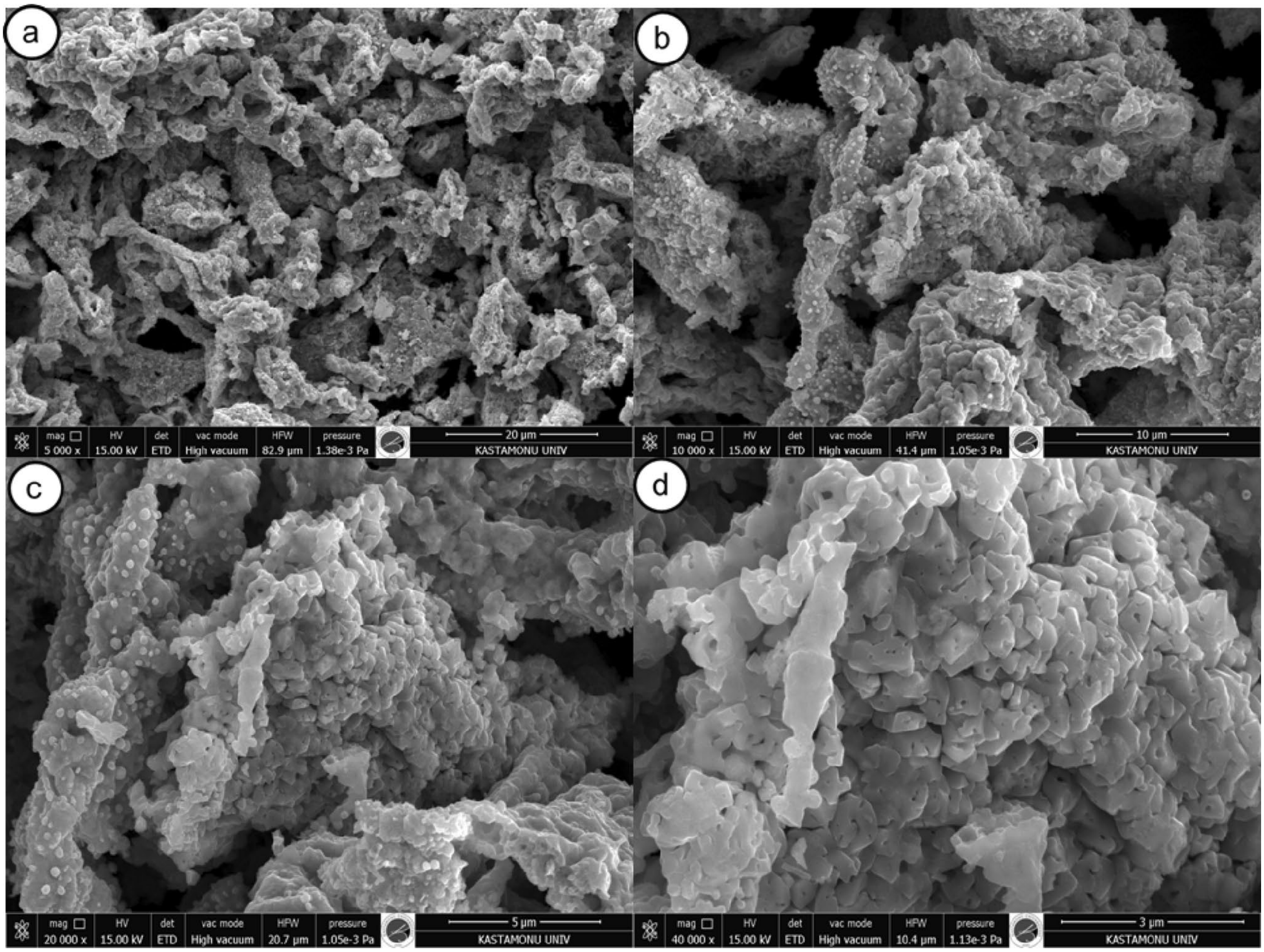

Fig. 3 SEM images of $CuFe_2O_4$ NPs for **a** 20-µm, **b** 10-µm, **c** 5-µm, **d** 3-µm magnifications

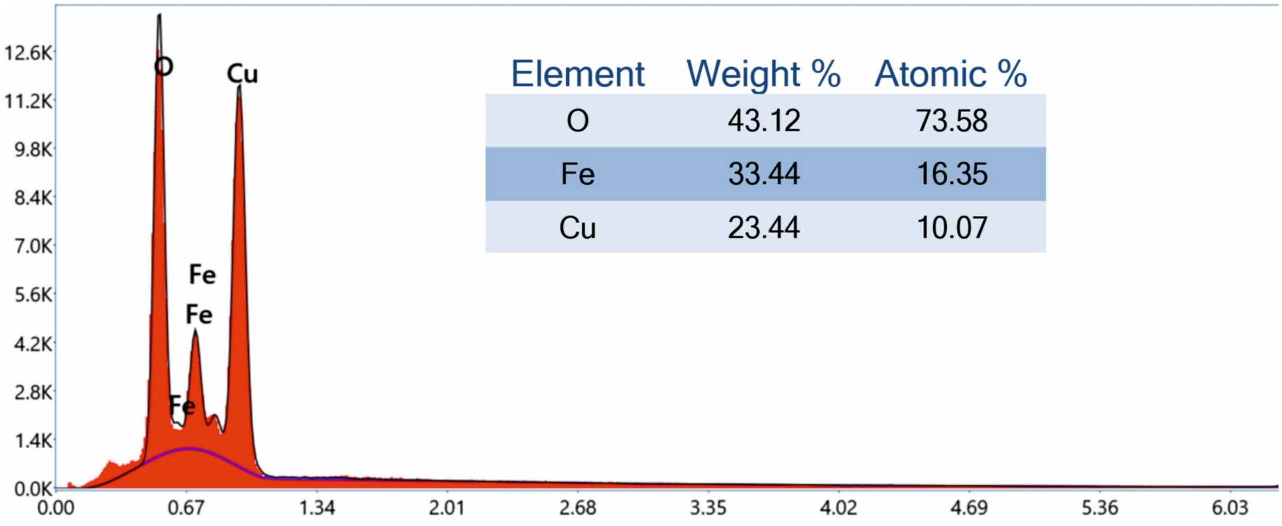

Element	Weight %	Atomic %
O	43.12	73.58
Fe	33.44	16.35
Cu	23.44	10.07

Fig. 4 EDS graph of $CuFe_2O_4$ NPs

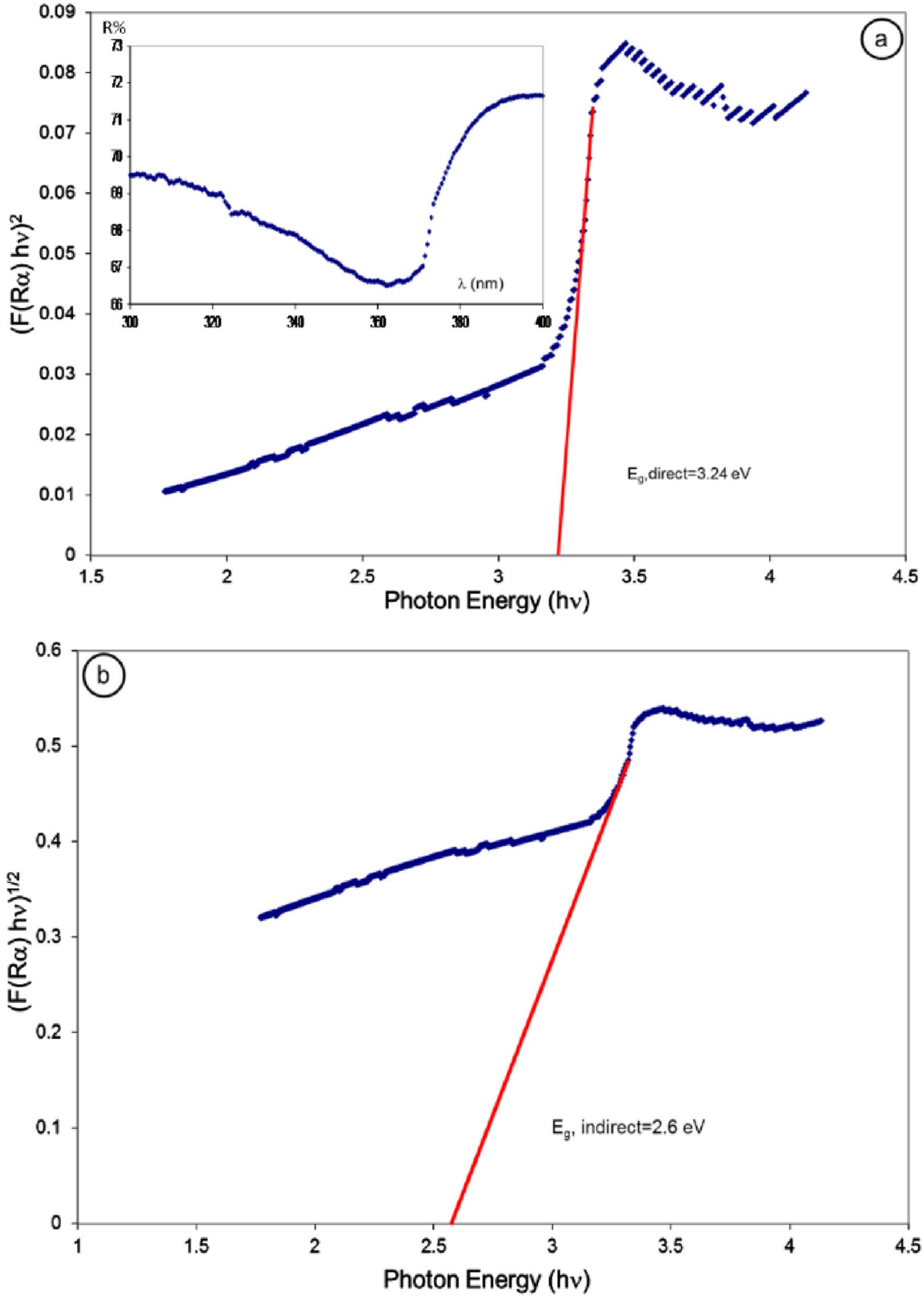

Fig. 5 The graphs of **a** $(F(R_\alpha)h\nu)^2$ and **b** $(F(R_\alpha)h\nu)^{1/2}$ against photon energy ($h\nu$) and the linear fit for the $CuFe_2O_4$ NPs. The dependence of R in the range 300 nm < λ ≤ 400 nm is presented in the inset of Fig. 4a

lattice strain, crystal size, and the size effect of substituted metals in Cu-spinel ferrite lattice.

3.4 Magnetic Behavior

The spinel ferrite $CuFe_2O_4$ NPs play an important role in materials science because of the following properties: chemical stability, mechanical hardness, low bandgap energy, visible light absorption capacity, and high saturation magnetization (Ms) values. To determine the characteristic magnetic nature of the Cu-Fe_2O_4 NPs, the magnetization versus magnetic field experiment have been performed at room temperature in the range of ± 1 Tesla. The variation of magnetization with respect to the applied magnetic field has presented in Fig. 6. As can be seen in the figure, *M-H* loop shows a *S*-shaped pointing to the soft ferromagnetic behavior. The results consisting of coercivity field (H_c) is obtained to be 1412 Oe.

The field dependence of the magnetization (M) close to the saturation value was calculated using the formula below [48]:

$$M = M_s[1 - \frac{\beta}{H^2}] \tag{7}$$

where the saturation magnetization is M_s, β is a parameter related to the magneto-crystalline anisotropy and the applied magnetic field is H. Inset of Fig. 6 illustrates the magnetization versus $1/H^2$. I determined β and M_s values of the $CuFe_2O_4$ NPs from the slope of the linear fitting and the interception with the *y*-axis, as 4.76×10^7 Oe^2 and 14.06 emu/g, respectively. Once I know the β value then the magnetic anisotropy constant (K_a) can be calculated using the following equation [48]:

$$K_a = M_s\sqrt{\frac{15\beta}{4}} \tag{8}$$

K value at room temperature is obtained as 1.9×10^5 erg/g. All magnetic quantities deduced in this study are almost in agreement with the literature related to the Fe-spinels [2, 45]. Thus, our $CuFe_2O_4$ NPs can be used in both industrial and biomedical fields.

3.5 Photocatalytic Properties

Oxidative stress leads to numerous pathologies such as altered endothelial cell function leading to vascular disorders, oxidative denaturation, hypertension, and also hemolysis [49, 50]. Reactive oxygen species (ROS) are one of the most important responsibilities of these pathologies which can also be used to degrade organic polluting agents like hydrocarbons, dyes, or pharmaceuticals in contaminated water [51–53]. In this study, CV, which is a common organic molecule in textile wastewater was used as a model organic molecule to diagnose the photocatalytic properties of $CuFe_2O_4$ NPs [54]. CV was also chosen due to its availability, low cost, high color intensity even at low

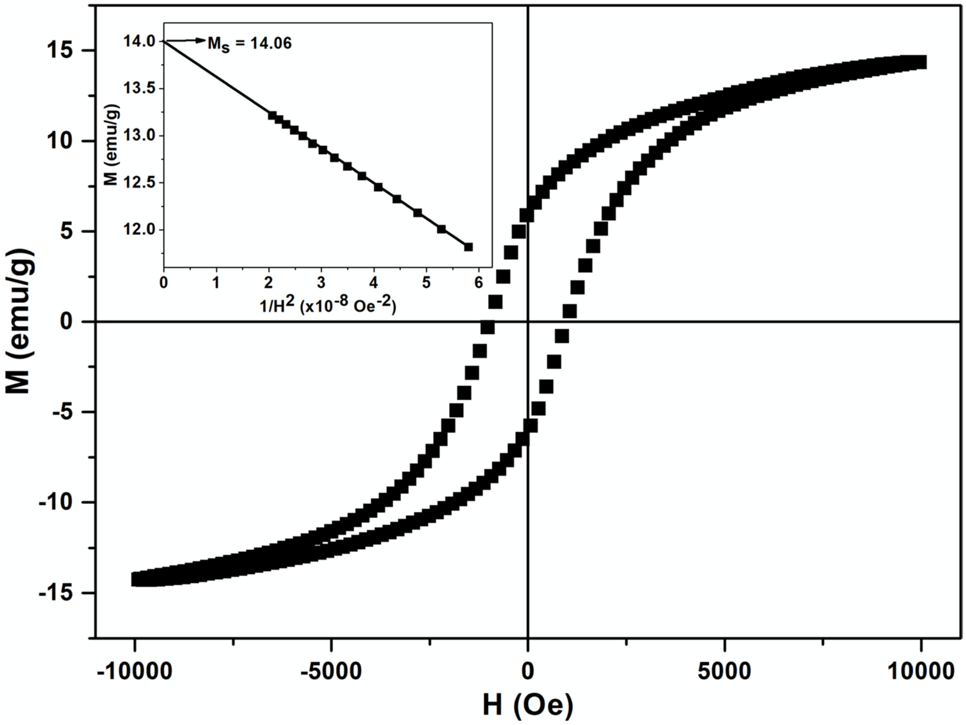

Fig. 6 M-H curves measured at $T = 300$ K for $CuFe_2O_4$ NPs. Inset shows the plots of M versus $1/H^2$ obtained in $CuFe_2O_4$ at $T = 300$ K

concentrations. Schematic representation of photocatalytic activity was shown in Fig. 7.

Variations in the UV–visible spectrum of non-photodegraded CV in aqueous suspension of $CuFe_2O_4$ and NPs with the variation of time were shown in Fig. 8. As can be seen from the figure, the absorption band intensity was gradually reduced with increase of time from 0 to 420 min. The intensity of the characteristic band at 591 nm weakened after 420 min under the effect of 254-nm irradiation indicating the degradation of CV by $CuFe_2O_4$ NPs.

The degradation percentage of CV was calculated using the equation given below.

$$\%\ degradation = [\frac{C_o - C_t}{C_o}] \times 100 \tag{9}$$

where C_o and C_t are is initial and at time t CV concentrations, respectively.

Bhukal et al. [55] used the sol–gel auto-combustion method to synthesize $Co_{0.6}Zn_{0.4}Cu_xFe_{(2-x)}O_4$ NPs. The data obtained from that study showed that as the Cu content of the obtained NPs increased, catalytic activity also increased. This was consistent with the results obtained from our study.

Although the band-gap value of $CoFe_2O_4$ in the study of Yalcin et al. [56] was lower than that of $CuFe_2O_4$, possible structural defects such as trap states may cause $CuFe_2O_4$ to have higher photocatalytic activity. Another possible reason

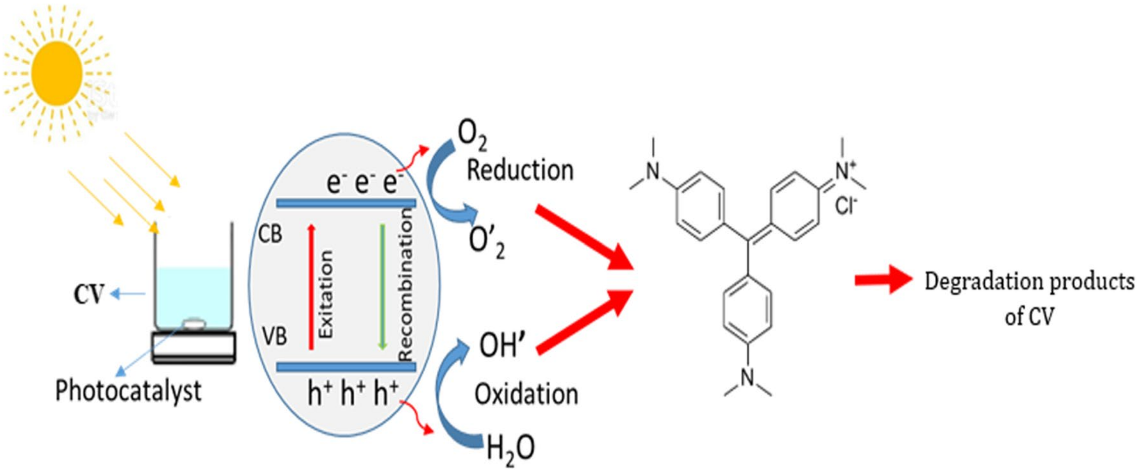

Fig. 7 Schematic representation of photocatalytic activity

Fig. 8 UV–vis spectra of CV versus wavelength in presence of $CuFe_2O_4$ under 254 nm irradiation

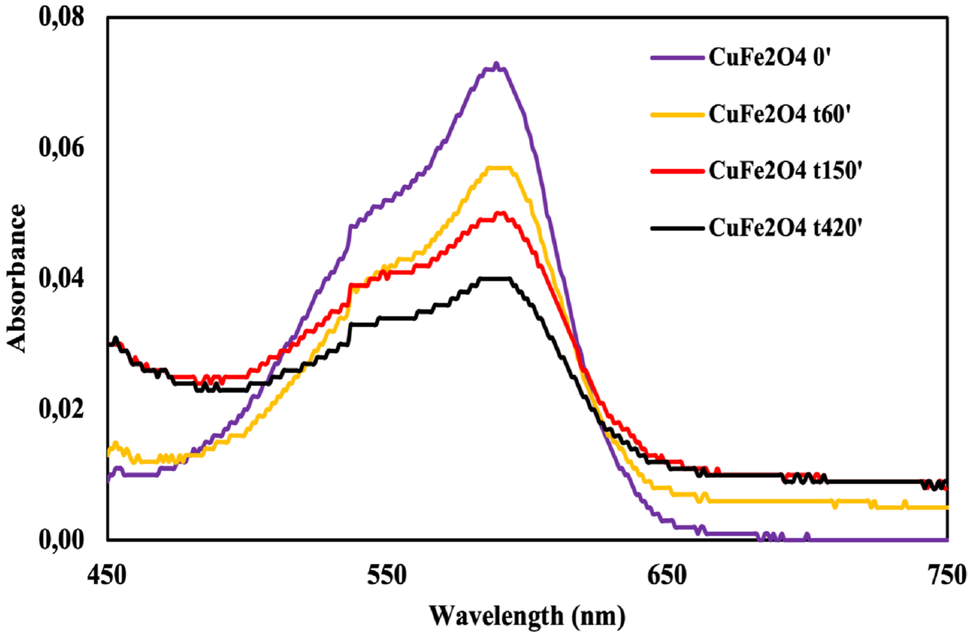

may be the strong orientation ability of Cu^{2+} ions in the octahedral structure.

The mechanism for the degradation of CV in presence of $CuFe_2O_4$ NPs follows the below-mentioned reactions.

Step 1 – Excitation of valence band electrons: In this step, valence band (*vb*) electrons are photo-excited by electromagnetic radiation possessing more energy comparison to the bandgap of $CuFe_2O_4$ NPs. Electrons migrate to a blank conduction band (*cb*) leaving equal numbers of holes in the valence band.

$$CuFe_2O_4 + h\nu \rightarrow CuFe_2O_4(e^-_{cb}) + CuFe_2O_4(h^+_{vb}) \tag{10}$$

Step 2 – Formation of ROS such as HO^* and O_2^{-*}: Migrated electrons to the surface of material reacts with O_2, H_2O, or HO^- to produce ROS.

$$CuFe_2O_4(e^-_{cb}) + O_2 \rightarrow O_2^{-*} \tag{11}$$

$$CuFe_2O_4(h^+_{vb}) + H_2O \rightarrow H^+ + HO^* \tag{12}$$

$$CuFe_2O_4(h^+_{vb}) + HO^- \rightarrow HO^* \tag{13}$$

Step 3 – Damping of the activity of O_2^{-*} and formation of HO_2^* radicals: During this step, other reactive intermediates such as hydrogen peroxide (H_2O_2) and hydroperoxyl radicals (HO_2^*) are formed.

$$O_2^{-*} + H^+ \rightarrow HO_2^* \rightarrow\rightarrow H_2O_2 + O_2 \tag{14}$$

$$H_2O_2 + O_2^{-*} \rightarrow HO^* + HO^- + O_2 \tag{15}$$

Step 4 – Degradation of organic molecules and closing down the photocatalytic cycle: During this step, the photocatalytic cycle is closed. Cu^{3+} sites react with hydroxyl ions and return to Cu^{2+}. Simultaneously, photocatalytic degradation of CV into less harmful molecules such as H_2O and CO_2 occur.

$$CuFe_2O_4(h^+_{vb}) + HO^- \rightarrow CuFe_2O_4 + HO^* \tag{16}$$

$$O_2^{-*}, HO^*, HO_2^* + CV \rightarrow \text{ Degradation products of CV} \tag{17}$$

Photocatalytic properties of $CuFe_2O_4$ NPs were investigated using three different kinetic models namely zero-order, first-order, and second-order, the equations describing each kinetic model are given in Eqs. 18–20 [57–60];

$$\text{Zero} - \text{order}: \; C_t = -kt + C_o \tag{18}$$

$$\text{First} - \text{order}: \; \ln\left(C_t\right) = -k_1\text{t} + \ln(C_o) \tag{19}$$

$$\text{Second} - \text{order}: \; \tfrac{1}{C_t} = k_2t + \tfrac{1}{C_o} \tag{20}$$

where k, k_1, and k_2 correspond to photocatalytic degradation rate constants.

All variables used in the calculation of kinetic parameters were determined using the calibration equation obtained from the CV calibration curve as seen in Fig. 9. Calculated

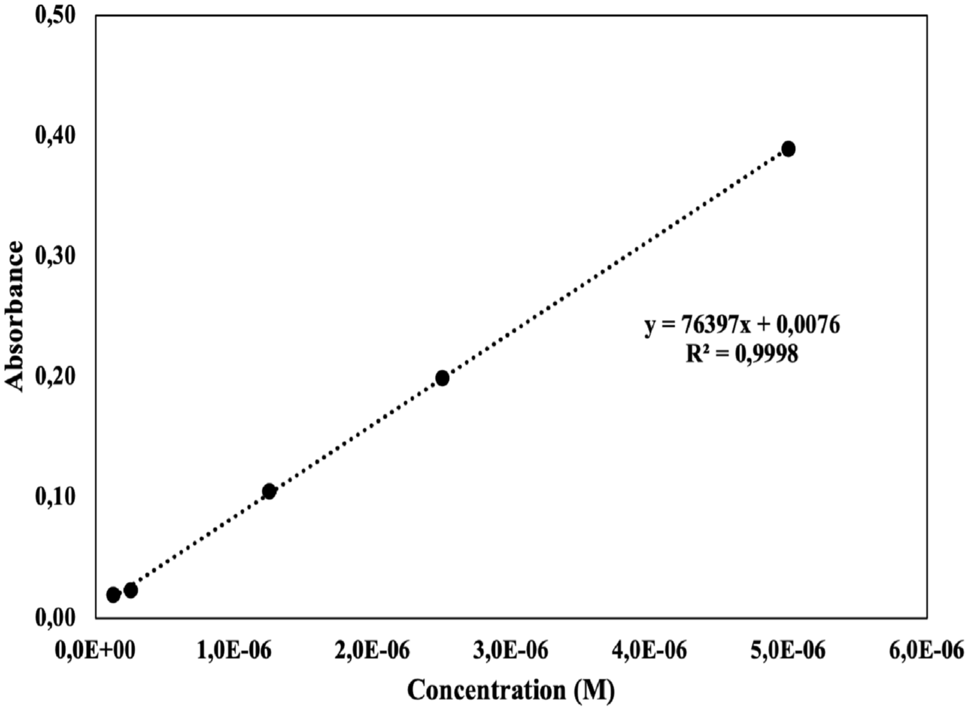

Fig. 9 Calibration graphic of CV

rate constants from each kinetic model as well as the correlation coefficient of each kinetic equation (R) were listed in Table 1. Fitting the results of photocatalysis tests on $\frac{1}{C_t}$ versus t graph gave best consistency with the experimental data. Low correlation coefficients obtained from C_t-t and $\ln(C_t)$- t graphics indicated the failure of zero-order and first-order kinetic models. Moreover, among the applied mathematical models, it was determined as the 2nd order kinetic model that gave the most consistent result in terms of calculated and theoretical CV concentrations (Table 1).

Table 1 Kinetic parameters of three kinetic models applied to interpret the $CuFe_2O_4$-triggered photodegradation of CV

Kinetic Model	Parameters	Value	Difference (%)
Zero-order	k_0	1.0E^{-10} mol/L min	
	R^2	0.9175	
	$C_{o,calculated}$	7.5E^{-7} M	70.04
First-order	k_1	1.5E^{-3} 1/min	
	R^2	0.9650	
	$C_{o,calculated}$	7.6E^{-7} M	69.76
Second-order	k_1	2755.6 L/mol min	
	R^2	0.9920	
	$C_{o,calculated}$	1.3E^{-7} M	47.60

Second-order photodegradation kinetics of CV and extent of the degradation of CV was given in Fig. 10a–b. The percentage of CV removed by $CuFe_2O_4$ NPs reaches 55.4% after 1440 min. Photocatalytic activity of $CuFe_2O_4$ NPs can be attributed to the possible structural defects or trap states and the strong orientation ability of Cu^{2+} ions in the octahedral structure [61]. Results represented the capability of $CuFe_2O4$ NPs to degrade CV, under 254-nm irradiation.

3.6 Blood Compatibility Tests

The main reason for the biological incompatibility between red blood cells and iron-containing NPs is due to the high activity of iron in chemical and biological processes. These unwanted interactions can be avoided by using ferrites for better hemocompatibility. In a related literature study,

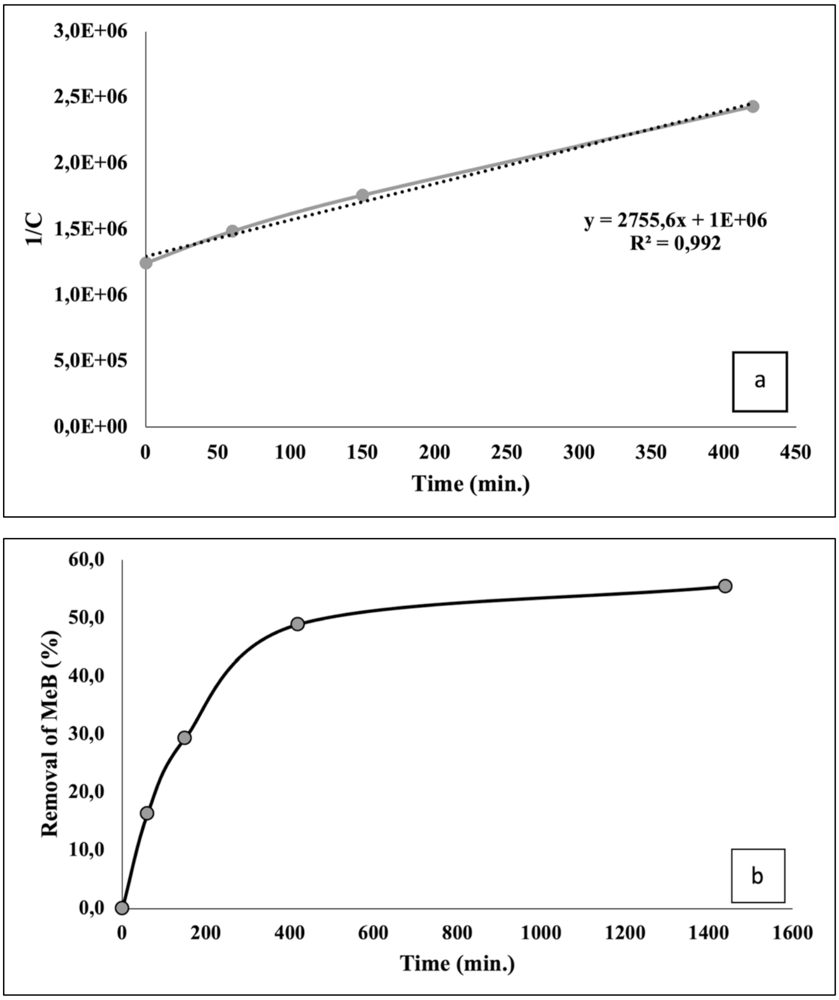

Fig. 10 **a** Second order photodegradation kinetics of CV and **b** extent of the degradation of CV

magnetic $CuFe_2O_4$ nanocrystals were used in the separation of histidine-rich proteins such as hemoglobin. Researchers focused on the selective binding capacity of hemoglobin by $CuFe_2O_4$ nanocrystals and reported 4475-mg hemoglobin adsorption for each 1 g of $CuFe_2O_4$ [62]. In another study, polyacrylic acrylic acid-coated $CuFe_2O_4$ NPs were used in selective separation of hemoglobin [63]. Special proteins can selectively be separated from blood to collect and analyze some biological molecules such as DNA which are present in blood in very low concentrations. These molecules are not easy to detect because of several interferences between abundant blood proteins such as hemoglobin. Chelating properties arising from the presence of ions such as Cu^{2+}, Co^{2+}, or Ni^{2+} cause gels, beads, or NPs to form covalent interactions with histidine-rich proteins. Among these, NPs have become very popular due to their surface properties, stability, and magnetic properties.

Hemolytic activity tests are the most applicable and scientifically accepted method that enables the determination of the biocompatibility properties of a newly synthesized material. In this study, I analyzed the hemolytic potentials of copper ferrites using healthy human erythrocytes. Figure 11 exhibits the UV–vis spectra of erythrocyte suspensions treated with PBS alone (control), $CuFe_2O_4$, NPs with two different (1.0 mg/ml and 5.0 mg/ml) concentrations. In blood samples treated with copper-containing ferrites, absorption peaks at 540 nm and 580 nm corresponding to oxyhemoglobin [64] completely disappeared (marked with arrows in Fig. 11).

Cu has a vital role by taking part in the structure of many enzymes and it is necessary for the synthesis of biological molecules like myelin, melanin, and hemoglobin [65]. Although being an essential micronutrient in metabolic processes, excessive concentrations of Cu induce toxic effects both in vivo and in vitro. Cu^{2+} ions show selective affinity towards the thiol group and tend to bond with –SH containing molecules like metallothioneins, glutathione, and hemoglobin. Copper is also suspected to cause the oxidation of cysteine to cystine [66, 67] and the formation of a copper-dicysteine complex $[(RS-)Cu^{2+}(-SR)]$ [68].

As shown by Fig. 11, the spectrum of $CuFe_2O_4$ NPs consisted of a shoulder centered at 370 nm, and an absorbance tail extending from 500 to 650 nm. These features are typical of square planar Cu(II) complexes with thiolate ligands [66]. The absorption peak at 415 nm got broader and showed a blue shift to 370-nm region indicating the possible interaction of copper and thiol (–SH) groups following the relevant studies in the literature [69]. Moreover, in all test tubes, the precipitate with a characteristic black color supplied obvious proof to designate the formation of heme–iron complexes [70]. MHb is mainly formed as a result of oxidation of Fe in the hemoglobin structure to 3 + state under the effect of oxidative stress. Based on this, it could be concluded that the high amount of ROS observed in the photocatalytic activity test results was also supported by the formation of MHb observed in blood compatibility trials. As it is mentioned in the introduction part, the copper is known as an essential micronutrient. It is also the co-factor of several enzymes involved in human metabolism, and presents toxic effects at a high concentration value. ROS formed by copper ferrite NPs causes the oxidation of hemoglobin to methemoglobin in the organism. Methemoglobin (MHb) is formed when the iron (Fe^{2+}) ions in heme oxidize to the ferric (Fe^{3+}) state, and the oxygen-carrying capacity of the molecule to tissues is significantly reduced. MHb can be generated by daily environmental exposure, as well as by chlorides, phenolic compounds, and various heavy metal ions [71–73]. In a normally functioning metabolic process, methemoglobin is re-converted to hemoglobin by being reduced by enzymatic reactions within cells. However, copper can disrupt

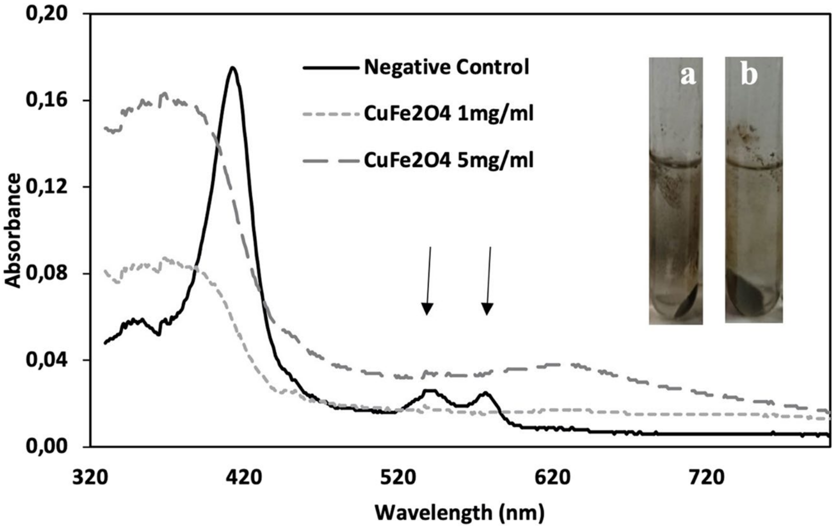

Fig. 11 UV–vis spectra of erythrocyte suspensions treated with PBS alone (negative control), $CuFe_2O_4$ NPs with two different concentrations. Inset: Digital photographs of erythrocyte-nanoparticle suspensions, **a** $CuFe_2O_4$ (1 mg/ml), **b** $CuFe_2O_4$ (5 mg/ml)

the functionality of those mechanisms by affecting the enzymatic activities [74].

Briefly, I observed copper-induced oxidation of heme and formation of methemoglobin with increasing $CuFe_2O_4$ concentrations. In conclusion, these ferrites can be considered as appropriate materials for biomedical applications such as magnetic hyperthermia due to their non-hemolytic effects. Our future work is to locate reducing agents such as curcumin, ascorbic acid, or glutathione to the nanoparticle structure and to reduce MHb to hemoglobin via non-enzymatic reactions directly.

4 Conclusion

The co-precipitation method using $FeN_3O_9.9H_2O$ and $Cu(NO_3)_2.6H_2O$ was used to synthesize $CuFe_2O_4$ spinel ferrites. Produced $CuFe_2O_4$ nanoparticles were almost chemically pure in terms of secondary phases and exhibited an agglomerated structure. The Cu-ferrite NPs have a cubic structure with a lattice parameter $\boldsymbol{a} = 8.45$ Å and a space group *Fd3m*. The direct and indirect gap energies of the Cu-ferrite NPs samples were deduced as 3.24 and 2.6 eV, respectively. The magnetic hysteresis graph (M-H) presents an *S*-shaped pointing to the soft ferromagnetic behavior with the coercivity field (H_c) value of 1412 Oe, saturation magnetization (Ms) value of 14.06 emu/gr. Besides the structural characterizations, the hemolytic activity has been studied for the synthesized $CuFe_2O_4$ NPs. Characteristics of the absorbance spectra obtained from hemolysis tests revealed the possible interactions of copper and thiol (–SH) groups. Moreover, the observation of the formation of a characteristic black precipitate in hemolytic activity tests was interpreted as clear evidence for the formation of heme–iron complexes in both $CuFe_2O_4$ samples. Photocatalytic activity measurements showed that, while $CuFe_2O_4$ NPs could degrade 55.4% of total CV after 1440 min. Both photocatalytic activity and hemolytic potential test results provided supporting data for ROS formation and the results agreed with each other. Among three kinetic models, second-order model showing the highest correlation coefficient was found as the most suitable model to explain the experimental photodegradation data. Higher photocatalytic activity of $CuFe_2O_4$ NPs was attributed to the possible structural defects such as trap states and the strong orientation ability of Cu^{2+} ions in the octahedral structure.

Acknowledgements I would like to thank Prof. Dr. B. Özçelik from Cukurova University and Prof.Dr.Lütfi Arda from Bahçeşehir University for their valuable contribution and discussions on the structural, physical and biological characterizations.

Author Contribution I have carried out all part of experiments and written the main manuscript text.

Funding No funding.

Data Availability The data used to support the findings of this study are available from the corresponding author upon request.

Declarations

Ethics Approval Not applicable.

Consent to Participate Not applicable.

Consent for Publication Not applicable.

Conflict of Interest The author declares no competing interests.

References

1. Maity, D., Sudame, A., Kandasamy, G. (2020). Superparamagnetic iron oxide nanoparticle-based drug delivery in cancer therapeutics. Nanobiotechnology in Diagnosis, Drug Delivery, and Treatment, 129–151, https://doi.org/10.1002/9781119671732.ch7.
2. Amiri, M., Akbari, A., Ahmadi, M., Pardakhti, A., & Salavati-Niasari, M. (2018). Synthesis and in vitro evaluation of a novel magnetic drug delivery system; pro-ecological method for the preparation of $CoFe_2O_4$ nanostructures. *Journal of Molecular Liquids, 249*, 1151.
3. Vajhadin, F., Mazloum-Ardakani, M., Raeisi, S., Hemati, M., Ebadi, A., Haghiralsadat, F., & Tofighi, D. (2022). Glutaraldehyde crosslinked doxorubicin promotes drug delivery efficiency using cobalt ferrite nanoparticles. *Colloids and Surfaces B: Biointerfaces, 220*, 112870.
4. Heiba, Z. K., Mohamed, M. B., Wahba, A. M., & Arda, L. (2015). Magnetic and structural properties of nanocrystalline cobalt-substituted magnesium–manganese ferrite. *Journal of Superconductivity and Novel Magnetism, 28*(8), 2517.
5. Yeganeh, F. E., Yeganeh, A. E., Far, B. F., Akbarzadeh, I., Quazi, S., & Safdar, M. (2022). In vitro cytotoxicity and anti-cancer drug release behavior of methionine-coated magnetite nanoparticles as carriers. *Medical Oncology, 39*(12), 252.
6. Wei, K., Huai, H.-X., Zhao, B., Zheng, J., Gao, G.-Q., Zheng, X.-Y., & Wang, C.-C. (2022). Facile synthesis of CoFe2O4 nanoparticles and their gas sensing properties. *Sensors and Actuators B: Chemical, 369*, 132279.
7. Elansary, M., Belaiche, M., Mouhib, Y., Lemine, O. M., Bentarhlia, N., & Bsoul, I. (2023). Novel biocompatible nanomaterial for biomedical application: Structural, morphological, magnetic, and in vivo toxicity investigations. *Ceramics International, 49*(3), 4551.
8. Sharma, S. K., Shrivastava, N., Rossi, F., Tung, L. D., & Thanh, N. T. K. (2019). Nanoparticles-based magnetic and photo induced hyperthermia for cancer treatment. *Nano Today, 29*, 100795.
9. Samrot, A. V., Sahithya, C. S., Selvarani, A. J., Purayil, S. K., & Ponnaiah, P. (2021). A review on synthesis, characterization and potential biological applications of superparamagnetic iron oxide nanoparticles. *Current Research in Green and Sustainable Chemistry, 4*, 100042.
10. Talebniya, S., Sharifi, I., Saeri, M. R., & Doostmohammadi, A. (2022). Study of cation distribution and magnetic properties of MFe2O4 (M = Fe Co, Zn, Mn, and Cu) nanoparticles. *Journal of Superconductivity and Novel Magnetism, 35*, 899.
11. Chaudhary, R. G., Potbhare, A. K., Tarik Aziz, S. K., Umekar, M. S., Bhuyar, S. S., & Mondal, A. (2021). Phytochemically

fabricated reduced graphene Oxide-ZnO NCs by Sesbania bispinosa for photocatalytic performances. *Materials Today: Proceedings, 36*, 756.

12. Umekar, M. S., Chaudhary, R. G., Bhusari, G. S., Mondal, A., Potbhare, A. K., & Sami, M. (2020). Phytoreduced graphene oxide-titanium dioxide nanocomposites using *Moringa oleifera* stick extract. *Materials Today: Proceedings, 29*, 709.
13. Umekar, M. S., Buhusari, G. S., Potbhare, A. K., Mondal, A., Kapgate, B. P., Desimone, M. F., & Chaudhary, R. G. (2021). Bioinspired reduced graphene oxide based nanohybrids for photocatalysis and antibacterial applications. *Current Pharmaceutical Biotechnology, 22*, 1759.
14. Sonkusare, V. N., Chaudhary, R. G., Bhusari, G. S., Mondal, A., Potbhare, A. K., Mishra, R. K., Juneja, H. D., & Abdala, A. A. (2020). Mesoporous octahedron-shaped tricobalt tetroxide nanoparticles for photocatalytic degradation of toxic dyes. *ACS Omega, 5*, 7823.
15. Nikazar, S., Barani, M., Rahdar, A., Zoghi, M., & Kyzas, G. Z. (2020). Photo-and magnetothermally responsive nanomaterials for therapy, controlled drug delivery and imaging applications. *Chemistry Select, 5*(40), 12590.
16. Arda, L., Dogan, N., & Boyraz, C. (2018). Effects of annealing temperature on microstructure and magnetic properties of Ni$_{0.05}$Zn$_{0.95}$Fe$_2$O$_4$ nanoparticles. *Journal of Superconductivity and Novel Magnetism, 31*(2), 365.
17. Satheeshkumar, M. K., Kumar, E. R., Indhumathi, P., Srinivas, C., Deepty, M., Sathiyaraj, S., Suriyanarayanan, N., & Sastry, D. L. (2020). Structural, morphological and magnetic properties of algae/CoFe2O4 and algae/Ag-Fe-O nanocomposites and their biomedical applications. *Inorganic Chemistry Communications, 111*, 107578.
18. Rathod, S. M., Chavan, A. R., Jadhav, S. S., Batoo, K. M., Hadi, M., & Raslan, E. H. (2021). Ag+ ion substituted CuFe2O4 nanoparticles: Analysis of structural and magnetic behavior. *Chemical Physics Letters, 765*, 138308.
19. Sharifianjazi, F., Moradi, M., Parvin, N., Nemati, A., Rad, A. J., Sheysi, N., Abouchenari, A., Mohammadi, A., Karbasi, S., Ahmadi, Z., Esmaeilkhanian, A., Irani, M., Pakseresht, A., Sahmani, S., & Asl, M. S. (2020). Magnetic CoFe2O4 nanoparticles doped with metal ions: A review. *Ceramics International., 46*(11), 18391.
20. Yang, Y. J., Jiang, C., Chen, S., Wang, N., Yang, P., Liu, M., & Cheng, Y. (2022). Direct growth of hierarchical CoFe2O4 flower-like nanoflake arrays on Ni foam for high performance asymmetrical supercapacitor. *Journal of Electroanalytical Chemistry, 918*, 116385.
21. Shahzad, K., Mushtaq, S., Rizwan, M., Khalid, W., Atif, M., Din, Fakhar Ud, Ahmad, N., Abbasi, R., & Ali, Z. (2021). Field-controlled magnetoelectric core-shell CoFe2O4@BaTiO3 nanoparticles as effective drug carriers and drug release in vitro. *Materials Science and Engineering: C, 119*, 111444.
22. Kumar, S., Ohlan, A., Kumar, P., & Verma, V. (2020). Improved electromagnetic interference shielding response of polyaniline containing magnetic nano-ferrites. *Journal of Superconductivity and Novel Magnetism, 33*(4), 1187.
23. Al-Juaid, A. A. (2023). La^{3+} substitution impact on structural, magnetic, and electrical properties of CoFe2O4 synthesized via sucrose auto-combustion. *Material Research Express, 10*(2), 026101.
24. Raimundo, R. A., Silva, V. D., Ferreira, L. S., Loureiro, F. J. A., Fagg, D. P., Macedo, D. A., Gomes, U. U., Gomes, R. M., Soares, M. M., & Morales, M. A. (2023). High magnetic moment of nanoparticle-sphere-like Co, Fe based composites and alloys prepared by proteic sol-gel synthesis: Structure, magnetic study and OER activity. *Journal of Alloys and Compounds, 940*, 168783.
25. Yalcin, B. (2022). Exploration of the potential of Co/Cu co-doped Fe$_2$O$_4$ for medical applications: Nanostructure, catalytic properties, and blood compatibility. *Journal of Nanoparticle Research, 24*, 271. https://doi.org/10.1007/s11051-022-05645-7
26. Chithra, M., Anumol, C. N., Argish, V., Sahu, B. N., & Sahoo, S. C. (2023). Magnetic properties of co-ferrite nanoparticles prepared by co-precipitation method. *Journal of Materials Science: Materials in Electronics, 34*, 806.
27. Lone, G. A., & Ikram, M. (2023). Role of Ni doping in magnetic dilution of Fe sublattice and in tailoring optical properties of CoFe$_2$O$_4$. *Journal of Alloys and Compounds, 934*, 167891.
28. Cheng, Y., Chen, J., Wang, T., Wu, Q., Shi, D., Zhang, Y., Chen, K., & Li, H. (2023). Magnetically-separable acid-resistant CoFe2O4@Polymer@MIL-100 core-shell catalysts for the acetalization of benzaldehyde and methanol. *Journal of Colloid and Interface Science, 629*, 571. Part A.
29. Li, X., Guan, G., Zhao, T., & Xiang, J. (2023). In-situ encapsulating ultrafine CoFe2O4 nanoparticle into porous N-doped carbon nanofiber membrane as self-standing anode for enhanced lithium storage performance. *Electrochimica Acta, 441*, 141787.
30. Karami, M., & Fathirad, F. (2023). Cobalt ferrite nanoparticles anchored on reduced graphene oxide nanoribbons (0D/1D CoFe2O4/rGONRs) as an efficient catalyst for hydrogen generation via NaBH4 hydrolysis. *Inorganic Chemistry Communications, 150*, 110552.
31. Wu, T. L., Tan, X. N., Nong, T. T., Pan, Y. J., Qiu, P. F., He, J. Q., Zhou, Y., Tan, X. C., Huang, Z. Y., & Han, L. (2023). Rational synthesis of bimetallic CoFe-MOF-74 grown on Ni foam converted into bamboo-shoot-like α-Co(OH)2/CoFe2O4 nanorods for high-performance supercapacitors. *Chemical Engineering Journal, 457*, 141238.
32. Guduru, R., Liang, P., Hadjikhani, A., Wang, P., Musaramthota, V., Hernandez, A. F., Arkook, B., Hong, J., & Khizroev, S. (2022). Magnetically controlled crystallographic properties of graphite sheets with self-assembled periodic arrays of magnetoelectric nanoparticles. *Applied Surface Science, 573*, 151455.

33 Shao, Z., Zeng, T., He, Y., Zhang, D., & Pu, X. (2019). A novel magnetically separable CoFe$_2$O$_4$/Cd$_{0.9}$Zn$_{0.1}$S photocatalyst with remarkably enhanced H2 evolution activity under visible light irradiation. *Chemical Engineering Journal, 359*, 485.

34. Ahmad, S. I. (2022). Nano cobalt ferrites: Doping, Structural, Low-temperature, and room temperature magnetic and dielectric properties – A comprehensive review. *Journal of Magnetism and Magnetic Materials, 562*, 169840.
35. Nikmanesh, H., Jaberolansar, E., Kameli, P., Varzaneh, A. G., Mehrabi, M., & Rostami, M. (2022). Structural and magnetic properties of CoFe2O4 ferrite nanoparticles doped by gadolinium. *Nanotechnology, 33*, 4.

36 Mngadi, S., Mokhosi, S., Singh, M., & Mdlalose, W. (2020). Chitosan-functionalized Mg0.5Co0.5Fe2O4 magnetic nanoparticles enhance delivery of 5-fluorouracil in vitro. *Coatings, 10*(5), 446.

37. Mohammadi, Z., Montazerabadi, A., Irajirad, R., Attaran, R. N., Abedi, H., Shaegh, S. A., & Sazgarnia, A. (2023). Optimization of cobalt ferrite magnetic nanoparticle as a theranostic agent: MRI and hyperthermia. *Magnetic Resonance Materials in Physics*. https://doi.org/10.1007/s10334-023-01072-4
38. Wang, H., Shen, J., Cao, G., Gai, Z., Hong, K., Debata, P. R., Banerjee, P., & Zhou, S. (2013). Multifunctional PEG encapsulated Fe3O4@silver hybrid nanoparticles: Antibacterial activity, cell imaging and combined photothermo/chemo-therapy. *Journal of Materials Chemistry B, 1*, 6225.
39. Shi, Z., Y. Zeng, X. Chen, F. Zhou, L. Zheng, G. Wang, G., ... & Yu, R. (2020). Mesoporous superparamagnetic cobalt ferrite nanoclusters: Synthesis, characterization, and application in drug

delivery. *Journal of Magnetism and Magnetic Materials*, *498*, 166222.

40. Ansari, S. M., Sinha, B. B., Phase, D., Sen, D., Sastry, P. U., Kolekar, Y. D., & Ramana, C. V. (2019). Particle size, morphology, and chemical composition controlled CoFe2O4 nanoparticles with tunable magnetic properties via oleic acid based solvothermal synthesis for application in electronic devices. *ACS Applied Nano Materials, 2*, 1828.
41 Sharifi, I., Zamanian, A., & Behnamghader, A. (2016). Synthesis and characterization of Fe0.6Zn0.4Fe2O4 ferrite magnetic nanoclusters using simple thermal decomposition method. *Journal of Magnetism and Magnetic Materials, 412*, 107.
42. Huang, Z.-b, Gao, P.-z, Zheng, H.-b, Liu, X.-p, Wen, J., & Rebrov, E. V. (2019). Magnetic enrichment behavior of monodispersed MFe2O4 nano ferrites (M = Mg, Ca, Ni Co, and Cu). *Ceramics International, 45*, 15980.
43. Coppola, P., da Silva, F. G., Gomide, G., Paula, F. L. O., Campos, A. F. C., Perzynski, R., Kern, C., Depeyrot, J., & Aquino, R. (2016). Hydrothermal synthesis of mixed zinc–cobalt ferrite nanoparticles: Structural and magnetic properties. *Journal of Nanoparticle Research, 18*, 1.
44. Fayazzadeh, S., Khodaei, M., Arani, M., Mahdavi, S. R., Nizamov, T., & Majouga, A. (2020). Magnetic properties and magnetic hyperthermia of cobalt ferrite nanoparticles synthesized by hydrothermal method. *Journal of Superconductivity and Novel Magnetism, 33*, 2227.
45. Özçelik, S., Yalçın, B., Arda, L., Santos, H., Sáez-Puche, R., Angurel, L. A., de la Fuente, G. F., & Özçelik, B. (2021). Structure, magnetic, photocatalytic, and blood compatibility studies of nickel nano ferrites prepared by laser ablation technique in distilled water. *Journal of Alloys and Compounds, 854*, 157279.
46. Sharmiladevi, P., Akhtar, N., Haribabu, V., Girigoswami, K., Chattopadhyay, S., & Girigoswami, A. (2019). Excitation wavelength independent carbon-decorated ferrite nanodots for multimodal diagnosis and stimuli responsive therapy. *ACS Applied BioMaterials, 2*(4), 1634.
47. Cullity, B. D. (1956). *Element of X-ray differaction*. Addison-Wesley Publishing Company Inc.
48. Fang, H. C., Yang, Z., Ong, C. K., Li, Y., & Wang, C. S. (1998). Preparation and magnetic properties of (Zn-Sn) substituted barium hexaferrite nanoparticles for magnetic recording. *Journal of Magnetism and Magnetic Materials, 187*, 129.
49. Adam, M., Murugavel, S., Bugyei-Twum, A., Narang, T., Jain, S., Pan, Y., ... & Singh, K.K. (2018). BRCA2 is a novel regulator of endothelial cell function and apoptosis following oxidative stress. *Atherosclerosis Supplements, 32*, 110.
50. Fanelli, C., & Zatz, R. (2011). Linking oxidative stress, the renin-angiotensin system, and hypertension. *Hypertension, 57*, 373.
51. Senol, S. D., Yalcin, B., Ozugurlu, E., & Arda, L. (2020). Structure, microstructure, optical and photocatalytic properties of Mn-doped ZnO nanoparticles. *Materials Research Express, 7*(1), 015079.
52. Yalçin, B., Akcan, D., Yalçin, I. E., Alphan, M. C., Özyigit, I. I., & Arda, L. (2020). Effect of Mg doping on morphology, photocatalytic activity, and related biological properties of $Zn_{1-x}Mg_xO$ nanoparticles. *Turkish Journal of Chemistry, 44*(4), 1177–1199.
53. Tosun, M., Senol, S. D., & Arda, L. (2020). Effect of Mn/Cu co-doping on the structural, optical, and photocatalytic properties of ZnO nanorods. *Journal of Molecular Structure, 1212*, 128071.
54. Mani, S., & Bharagava, R. N. (2016). Exposure to crystal violet, its toxic, genotoxic, and carcinogenic effects on environment and its degradation and detoxification for environmental safety. *Reviews of Environmental Contamination and Toxicology, 237*, 71.
55. Bhukal, S., & Singhal, S. (2014). Magnetically separable copper substituted cobalt–zinc nano-ferrite photocatalyst with enhanced photocatalytic activity. *Materials Science in Semiconductor Processing, 26*, 467.
56. Yalcin, B., Özçelik, S., Icin, K., Senturk, K., Özçelik, B., & Arda, L. (2021). Structural, optical, magnetic, photocatalytic activity and related biological effects of CoFe2O4 ferrite nanoparticles. *Journal of Materials Science: Materials in Electronics, 32*(10), 13068.
57. Rahman, Q. I., Ahmad, M., Misra, S. K., & Lohani, M. (2013). Effective photocatalytic degradation of rhodamine B dye by ZnO nanoparticles. *Materials Letters, 91*, 170.
58. Hou, X., Feng, J., Liu, X., Ren, Y., Fan, Z., Wei, T., & Zhang, M. (2011). Synthesis of 3D porous ferromagnetic NiFe2O4 and using as novel adsorbent to treat wastewater. *Journal of Colloid and Interface Science, 362*(2), 477.
59. Matouq, M. A., Al-Anber, Z. A., Tagawa, T., Aljbour, S., & Al-Shannag, M. (2008). Degradation of dissolved diazinon pesticide in water using the high frequency of ultrasound wave. *Ultrasonics Sonochemistry, 15*(5), 869.
60. Rani, M., Shanker, U., & Chaurasia, A. K. (2017). Catalytic potential of laccase immobilized on transition metal oxides nanomaterials: Degradation of alizarin red S dye. *Journal of environmental chemical engineering, 5*(3), 2730.
61. Gottesman, R., Peracchi, I., Gerke, J. L., Irani, R., Abdi, F. F., & van de Krol, R. (2022). Shining a hot light on emerging photo absorber materials: The power of rapid radiative heating in developing oxide thin-film photoelectrodes. *ACS Energy Letters, 7*, 514.
62. Zheng, J., Lin, Z., Liu, W., Wang, L., Zhao, S., Yang, H., & Zhang, L. (2014). One-pot synthesis of $CuFe_2O_4$ magnetic nanocrystal clusters for highly specific separation of histidine-rich proteins. *Journal of Materials Chemistry B, 2*(37), 6207.
63 Liu, Y., Wang, Y., Yan, M., & Huang, J. (2017). Selective removal of hemoglobin from blood using hierarchical copper shells anchored to magnetic nanoparticles. *BioMed Research International, 2017*, 7309481. https://doi.org/10.1155/2017/7309481
64. Gorbatova, N., Gasanova, E., Zolotov, S., Sirotkin, A., Kuzmin, G., Tertychny, A., Stankova, N., Remmennicova, M., & Tikhonevich, O. (2022). Experimental confirmation of the promising selective use of “green” laser radiation for photo thermolysis of hemoglobin-containing tissues. *Lasers in Medical Science, 37*, 225.
65. Nima, R. S., Ablaa, H. A., & Mohammed, H. J. (2018). The relationship between blood counts and serum levels of zinc and copper in children with β-thalassemia living in Najaf Governorate, in Iraq. *Research Journal of Pharmacy and Technology, 11*(10), 4640.
66. Cavallini, D., De Marco, C., Duprè, S., & Rotilio, G. (1969). The copper-catalyzed oxidation of cysteine to cystine. *Archives of Biochemistry and Biophysics, 130*, 354.
67. Ishii, T., & Mann, G. E. (2014). Redox status in mammalian cells and stem cells during culture in vitro: Critical roles of Nrf2 and cystine transporter activity in the maintenance of redox balance. *Redox Biology, 2*, 786.
68. Rigo, A., Corazza, A., di Paolo, M. L., Rossetto, M., Ugolini, R., & Scarpa, M. (2004). Interaction of copper with cysteine: Stability of cuprous complexes and catalytic role of cupric ions in anaerobic thiol oxidation. *Journal of Inorganic Biochemistry, 98*(9), 1495.
69. Shanmugaraj, K., & John, S. A. (2018). Inner filter effect-based selective detection of picric acid in aqueous solution using

green luminescent copper nanoclusters. *New Journal of Chemistry, 42*(9), 7223.

70. Zimmerman, D., Dienes, J., Abdulmalik, O., & Elmer, J. J. (2016). Purification of diverse hemoglobins by metal salt precipitation. *Protein Expression and Purification, 125*, 74.
71. Pichert, A., & Arnhold, J. (2015). Interaction of the chlorite-based drug WF10 and chlorite with hemoglobin, methemoglobin and ferryl hemoglobin. *Archives of Biochemistry and Biophysics, 585*, 82.
72. Shen, H. M., Zhu, G. Y., Yu, W. B., Wu, H. K., Ji, H. B., Shi, H. X., & She, Y. B. (2015). Surface immobilization of β-cyclodextrin on hybrid silica and its fast adsorption performance of p-nitrophenol from the aqueous phase. *RSC Advances, 5*(103), 84410.
73. Gradinaru, A. C., Solcan, G., Spataru, M. C., Hritcu, L. D., Burtan, L. C., & Spataru, C. (2019). The Ecotoxicology of heavy metals from various anthropogenic sources and pathways for their bioremediation. *Revista De Chimie, 70*(7), 2556.
74. Shen, S. C., & Ley, A. B. (1954). Methemoglobin formation in human blood by cobalt in vitro. *The Journal of Clinical Investigation, 33*(11), 1560.

Publisher's Note Springer Nature remains neutral with regard to jurisdictional claims in published maps and institutional affiliations.

Springer Nature or its licensor (e.g. a society or other partner) holds exclusive rights to this article under a publishing agreement with the author(s) or other rightsholder(s); author self-archiving of the accepted manuscript version of this article is solely governed by the terms of such publishing agreement and applicable law.